



Heterogeneous & Homogeneous & Bio- & Nano-

CHEM **CAT** CHEM

CATALYSIS

Accepted Article

Title: Tuning the facet proportion of Co₂C nanoprisms for Fischer-Tropsch synthesis to olefins

Authors: Liangshu Zhong, Yunlei An, Tiejun Lin, Kun Gong, Xinxing Wang, Hui Wang, and Yuhan Sun

This manuscript has been accepted after peer review and appears as an Accepted Article online prior to editing, proofing, and formal publication of the final Version of Record (VoR). This work is currently citable by using the Digital Object Identifier (DOI) given below. The VoR will be published online in Early View as soon as possible and may be different to this Accepted Article as a result of editing. Readers should obtain the VoR from the journal website shown below when it is published to ensure accuracy of information. The authors are responsible for the content of this Accepted Article.

To be cited as: *ChemCatChem* 10.1002/cctc.201902273

Link to VoR: <http://dx.doi.org/10.1002/cctc.201902273>

WILEY-VCH

www.chemcatchem.org



Tuning the facet proportion of Co₂C nanoprisms for Fischer-Tropsch synthesis to olefins

Yunlei An,^[a,b] Tiejun Lin,^[a] Kun Gong,^[a,c] Xinxing Wang,^[a] Liangshu Zhong,^{*[a,d]} Hui Wang,^[a] Yuhan Sun^{*[a,d]}

[a] CAS Key Laboratory of Low-Carbon Conversion Science and Engineering, Shanghai Advanced Research Institute, Chinese Academy of Sciences, Shanghai 201203, PR China
E-mail for L. S. Zhong: zhongls@sari.ac.cn; E-mail for Y. H. Sun: sunyh@sari.ac.cn

[b] University of the Chinese Academy of Sciences, Beijing 100049, PR China

[c] College of Environmental and Chemical Engineering, Shanghai University, Shanghai 200444, PR China

[d] School of Physical Science and Technology, ShanghaiTech University, Shanghai 201203, PR China

Supporting information for this article is given via a link at the end of the document.

Abstract: Cobalt carbide (Co₂C) exhibits strong facet effect for Fischer-Tropsch to olefins (FTO) reaction. Herein, we report that the facet proportion of Co₂C nanostructures can be tuned effectively by incorporating and altering the Mn content in the CoMn composite oxide as catalyst precursor. With the addition of Mn promoter, the Co₂C nanoprisms with exposed (020) and (101) facets are generated under reaction conditions. In addition, the facet proportion of Co₂C(020) facet can be effectively improved by enhancing the Mn/Co ratio. With the increase of facet proportion of Co₂C(020)/Co₂C(101) ratio, the as-obtained Co₂C nanoprisms exhibit higher intrinsic activity and lower methane selectivity during the syngas conversion process. Kinetic experiments also demonstrate that the apparent activation energy (E_a) for CO conversion is significantly reduced as increasing the facet proportion of Co₂C(020). This work provides a simple and feasible way to tune the exposed facet proportion for the rational design of Co₂C nanocatalyst for FTO reaction.

Introduction

Fischer-Tropsch synthesis (FTS) is widely applied to produce fuels and value-added chemicals from syngas (H₂ and CO) derived from various carbon-containing resources including coal, natural gas and biomass.^[1] The goal in the traditional FTS reaction using Fe, Co and Ru based catalysts is to develop a suitable catalyst with high activity and high selectivity toward C₅₊ hydrocarbons.^[2] It is generally believed that Fischer-Tropsch synthesis is a surface catalyzed structure-sensitive reaction, and the catalytic performance is strongly influenced by the morphology and exposed facets of the active phase.^[3] For Fe-based catalysts, iron carbide (FeC_x) is easily formed under FT reaction conditions, and different exposed facets of FeC_x possess different energy barriers for CO or H₂ activation. It was found that direct CO dissociation was the preferred pathway for CO activation on the terrace-like χ -Fe₅C₂ (510) facet, while H-assisted CO dissociation was the preferred one on the step-like χ -Fe₅C₂ (010) and (001) surfaces.^[4] Similarly, Co⁰ as the active phase for Co-based FT reaction also possesses strong facet effect. Co⁰ may exist in the form of hexagonal close-packed (HCP) phase or face-centered cubic (FCC) phase. Based on

theory study, HCP-Co was belonged to the D_{3h} point group and it exhibited a dihedral-like shape with two closed packed (0001) facets, while FCC-Co had an octahedron-like shape composed of (100), (110), (310) and (111) facets. In addition, the reaction rates for (11–21), (10–11), (10–12), and (11–20) facets of HCP-Co were higher than that for the exposed facets of FCC-Co.^[5] During the FT reaction process, many products including paraffins, olefins and oxygenates are generated simultaneously. For the traditional FT catalysts, paraffins are the main products with ASF distribution. In order to make the FT technology more economical, it is necessary to increase the selectivity to value-added chemicals. Lower olefins (C₂₋₄), which are key building blocks in chemical industry, are traditionally produced from catalytic cracking of hydrocarbon feedstocks from petroleum reserves^[6]. Fischer-Tropsch to olefins (FTO) is a promising route for direct production of olefins from syngas.^[6-7] Iron carbide is recognized as the active phase for Fe-based FTO reaction and the effect of various promoters on catalytic performance are widely investigated.^[8] It was found that the addition of Na and S played key role to improve the catalytic performance for FTO.^[9] In addition, Zn as promoter was also often used to modify the nature of Fe-based FTO catalysts. Zhai et al prepared FeZn-Na catalysts via co-precipitation method and proposed that Zn promoter could change the size of Fe phase as it acted as a structure promoter.^[10] Liu et al found that Mn promoter could accelerate the formation of θ -Fe₃C as the active phase with high selectivity toward lower olefins.^[11] In addition, the C₁ formation was significantly suppressed and the formation of C₅₊ product was favored after incorporation of Mn into Fe-based catalysts for syngas conversion.^[12]

In our previous work, a new kind of Co₂C-based catalyst was explored to exhibit high activity with high olefins selectivity and low CH₄ selectivity for syngas conversion at mild reaction conditions.^[13] Although the formation of Co₂C was often responsible for the deactivation of cobalt-based FTS reaction,^[14] we found that Co₂C nanoprisms with exposed facets of (020) and (101) were very promising for FTO reaction. Furthermore, we found that Na promoter could improve the formation rate of Co₂C.^[15] In addition, it was found that Mn promoter was important in modifying the active metal properties, and the addition of Mn could increase the reaction rate and enhance the

olefins selectivity and olefin/paraffin (O/P) ratio.^[16] We also investigated the effect of the Mn promoter and found that Mn could combine with Co element to form $\text{Co}_x\text{Mn}_{1-x}\text{O}$ spinel, which was the essential precursor for the formation of Co_2C nanoprisms under FTO reaction conditions.^[16] In addition, density functional theory (DFT) calculations indicated that Co_2C possessed strong facet effect in syngas conversion, and different facets of Co_2C possessed different catalytic performance. For example, the $\text{Co}_2\text{C}(020)$ facet was highly active for CO dissociation and possessed the highest effective barrier for CH_4 formation. Compared with $\text{Co}_2\text{C}(020)$ facet, the barrier for CO dissociative adsorption was higher on the $\text{Co}_2\text{C}(101)$ surface, and the $\text{Co}_2\text{C}(101)$ was more active for CH_4 formation^[17]. However, further experimental results are still needed to reveal the facet effect of Co_2C in syngas conversion. Co_2C nanoprisms are composed of $\text{Co}_2\text{C}(020)$ and $\text{Co}_2\text{C}(101)$ facets, it seems feasible to tune the catalytic performance via control the preferential facet of Co_2C nanoprisms. Herein, we investigated the role of Mn in controlling the proportion of $\text{Co}_2\text{C}(020)$ facet in Co_2C nanoprisms in detail. The corresponding changes in the catalytic performance for FTO reaction as well as kinetic parameters were correlated with Co_2C nanostructure.

Results and Discussion

Structure characterization

ICP and BET

The actual metal contents of Co and Mn for various catalysts with different Mn/Co ratios were determined by ICP-OES as summarized in Table 1. The molar ratio of Mn/Co was close to the nominal composition. For all of the studied catalysts, a small quantity of Na existed in various CoMn catalysts, which could accelerate the formation of Co_2C .^[15]

The BET surface area of the calcined and reduced samples was measured by N_2 physisorption as shown in Table 1. For the calcined catalysts, the specific surface area increased with increasing of Mn content as Mn could improve the dispersion of Co. For the reduced catalysts, once the Mn promoter was added, the BET surface area was raised from $18.7 \text{ m}^2/\text{g}$ (Co_3O_4) to $98.3 \text{ m}^2/\text{g}$ (Co_3Mn_1), then decreased to $43.4 \text{ m}^2/\text{g}$ with further increasing of Mn content.

Table 1. Elements analysis and surface properties of various catalysts.

Catalyst	ICP (wt%)			BET (m^2/g)	
	Co	Mn	Mn/Co (M/M)	Calcined	Reduced
Co_3O_4	78.4	/	0	76.0	18.7
Co_3Mn_1	57.3	16.0	0.30	130.0	98.3
Co_2Mn_1	48.7	22.2	0.49	136.6	91.1
Co_1Mn_1	34.5	31.3	0.97	158.2	45.7
Co_1Mn_2	22.2	40.4	1.96	168.6	43.4
Co_1Mn_3	16.8	45.5	2.94	160.6	51.1

XRD

The XRD patterns of various CoMn samples after reduction and reaction were shown in Figure 1. It was found that the Co species existed in different phases at different stages. For the reduced Co_3O_4 catalyst without Mn addition, the peaks were mainly attributed to Co^0 and CoO (Figure 1a). Besides, the results for the spent Co_3O_4 sample revealed that only Co_2C phase at 2θ of 37.0° , 41.3° , 42.6° , 45.7° and 56.6° could be detected (Figure 1b), suggesting that Co species were all transformed into Co_2C . However, all the reduced CoMn samples showed the characteristic peak of $\text{Co}_x\text{Mn}_{1-x}\text{O}$ phase (Figure 1a), which was the precursor for the formation of Co_2C nanoprisms.^[16] For the spent Co_3Mn_1 , Co_2Mn_1 and Co_1Mn_1 catalysts, both MnCO_3 and Co_2C phase co-existed. However, MnCO_3 , $\text{Co}_x\text{Mn}_{1-x}\text{O}$, MnO and Co_2C phases were observed in the spent Co_1Mn_2 and Co_1Mn_3 catalysts, and the peak intensity of MnCO_3 phase for the spent Co_1Mn_3 catalyst was very weak. In addition, the Co_2C phase showed different crystal planes intensities for various spent samples.

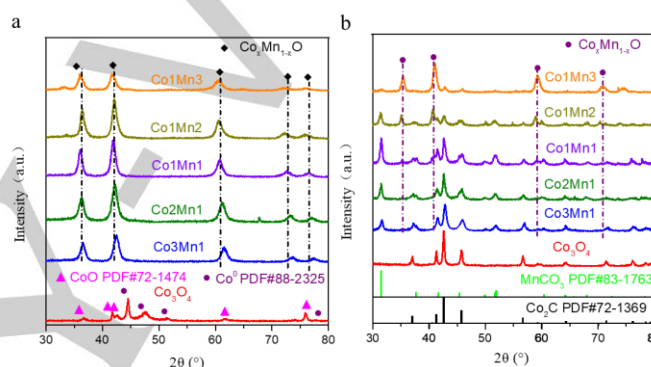


Figure 1. X-ray diffraction patterns for various catalysts with different Mn/Co ratio after reduction (a) and reaction (b). The reduction process was under 10 vol % CO/N_2 - 300°C . The catalytic test was carried out at a H_2/CO ratio of 0.5, 250°C , 5 bar and WHSV of $2000 \text{ ml}\cdot\text{g}^{-1}\cdot\text{h}^{-1}$.

The contents and average crystallite size of Co_2C after reaction were calculated as shown in Table 2, Figure S1 and Figure S2. The content of Co_2C showed the following sequence: $\text{Co}_3\text{O}_4 > \text{Co}_3\text{Mn}_1 > \text{Co}_2\text{Mn}_1 > \text{Co}_1\text{Mn}_1 > \text{Co}_1\text{Mn}_2 > \text{Co}_1\text{Mn}_3$. As for the crystallite sizes of Co_2C , the maximum size of 31.6 nm could be found for the spent Co_3O_4 catalyst. With doping of Mn promoter, the crystallite size of Co_2C decreased obviously to 18.5 nm (Co_3Mn_1), then the size seemed to decline slightly to 15.3 nm with further increasing of Mn content. Obviously, the addition of Mn promoter could enhance the dispersion of Co species and increase the nucleation number of Co_2C . The proportion of (020) facet in Co_2C was also calculated in Table S1, Table S2 and Table 2. The specific surface area proportion of $\text{Co}_2\text{C}(020)$ facet was calculated based on the model method, as shown in Figure S2. The change of surface area proportion of $\text{Co}_2\text{C}(020)$ showed an increasing tendency with the increasing of Mn/Co ratio. For example, the surface area proportion of $\text{Co}_2\text{C}(020)$ facet raised from 18.2% to 25.1% as improving the Mn/Co ratio from 0.33 to 3. Furthermore, the probability of exposed $\text{Co}_2\text{C}(101)$ and (020) facets was also calculated according to the means proposed by Huo et al.^[18] based on the XRD results. As shown in Table 2 and Table S2, the relative value (I/L_p) of $\text{Co}_2\text{C}(101)$ facet decreased gradually with the increasing of Mn/Co ratio. However, the relative value (I/L_p) for $\text{Co}_2\text{C}(020)$ facet increased. And the

relative value for (020)/(101) increased from 1.7 for Co_3O_4 to 13.2 for Co1Mn3 .

Table 2 Content of Co_2C , crystallite size of Co_2C , proportion of $\text{Co}_2\text{C}(020)$ and relative value (I/L_p) for (020)/(101) for various spent CoMn catalysts with different Mn/Co ratio.

Catalysts	Content of Co_2C (%)	Crystallite Size of Co_2C (nm)	Proportion of $\text{Co}_2\text{C}(020)$ facet (%)	(020)/(101) {Relative (I/L_p)}
Co_3O_4	100	31.6		1.7
Co3Mn1	54	18.5	18.2	2.0
Co2Mn1	48	17.7	18.9	3.1
Co1Mn1	36	18.0	21.7	5.0
Co1Mn2	29	17.9	24.0	10.0
Co1Mn3	20	15.3	25.1	13.2

H_2 -TPR

The reduction behavior of various CoMn samples with different Mn/Co ratio was studied by H_2 -TPR analysis (Figure 2). The unpromoted Co_3O_4 catalyst showed two step reduction pattern: $\text{Co}_3\text{O}_4 \rightarrow \text{CoO}$ at 158–270 °C, and $\text{CoO} \rightarrow \text{Co}^0$ at the temperature above 270 °C. With the increasing of Mn content, the H_2 consumption peaks significantly shifted toward higher temperature, suggesting that the addition of Mn hindered the reduction of Co species. In previous work, Guse and Salazar-Contreras et al also proposed that the formation of a stable Co-Mn spinel hindered the formation of metallic Co during the reduction process, even at a low content of Mn.^[19] In addition, there were only two peaks appeared in Co_3O_4 catalyst. However, a new peak located at 200 °C–300 °C appeared in the TPR profiles was observed with Mn addition, which could be attributed to the reduction process of $\text{Co}_x\text{Mn}_{1-x}\text{O}$.^[17]

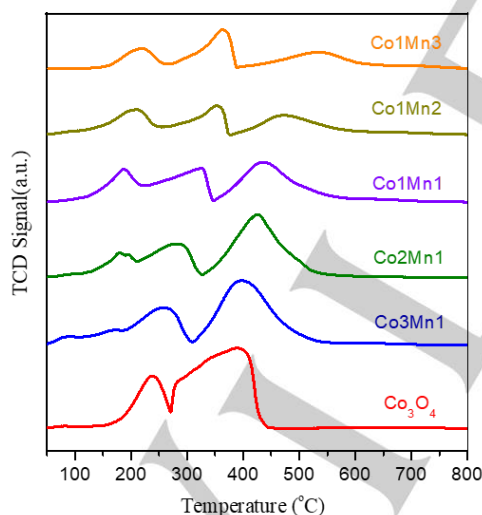


Figure 2. H_2 -TPR profiles for various catalysts with different Mn/Co ratio.

TEM

Transmission electron microscopy (TEM) images of the spent samples with different Mn/Co ratio were displayed in Figure 3. Co_2C nanospheres were found in the spent Co_3O_4 catalyst and the lattice distance of 1.98 Å was assigned to the $\text{Co}_2\text{C}(210)$ facet. In addition, serious sintering occurred for the spent Co_3O_4 catalysts. A large amount of Co_2C nanoprisms with exposed (101) and (020) facets were found for the spent samples of

Co3Mn1 , Co2Mn1 , Co1Mn1 , Co1Mn2 and Co1Mn3 . The lattice fringe of 2.18 Å was ascribed to $\text{Co}_2\text{C}(020)$ facet and 2.12 Å was matched with $\text{Co}_2\text{C}(111)$ plane. In addition, the $\text{Co}_2\text{C}(020)$ facet presented in Figure 3 seemed to grow larger with increasing of Mn content, which was consistent with the XRD results.

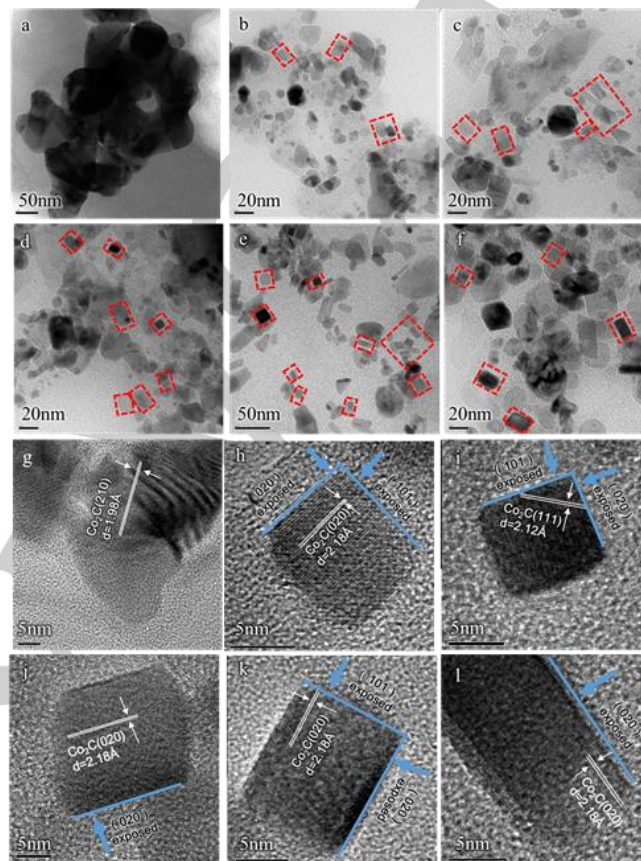


Figure 3. TEM (a-f) and HRTEM (g-l) images of various spent CoMn catalysts with different Mn/Co ratio. (a, g): Co_3O_4 ; (b, h): Co3Mn1 ; (c, i): Co2Mn1 ; (d, j): Co1Mn1 ; (e, k): Co1Mn2 ; (f, l): Co1Mn3 . Reaction conditions: 250 °C, 5 bar, $\text{H}_2/\text{CO}=0.5$, and WHSV of 2000 $\text{ml}\cdot\text{g}^{-1}\cdot\text{h}^{-1}$.

Catalytic performance

The catalytic performance of various CoMn catalysts at steady state was presented in Table 3. The presence of Mn promoter greatly altered the catalytic activity and product selectivity during FTO process. Once introducing the Mn promoter, CO conversion greatly increased from 6.1 C% for Co_3O_4 to 32.9 C% for Co3Mn1 . The CTY raised from 0.4×10^{-6} mol $\text{CO}/\text{g}_{\text{Co}_2\text{C}}\cdot\text{s}$ to 7.6×10^{-6} mol $\text{CO}/\text{g}_{\text{Co}_2\text{C}}\cdot\text{s}$, and reaction rate increased from 0.33×10^{-7} mol $\text{CO}/\text{m}^2_{\text{Co}_2\text{C}}\cdot\text{s}$ to 1.01×10^{-7} mol $\text{CO}/\text{m}^2_{\text{Co}_2\text{C}}\cdot\text{s}$. Furthermore, CH_4 selectivity decreased from 33.7 C% for Co_3O_4 to 11.9 C% for Co3Mn1 . The above results agreed well with our previous conclusion that the Co_2C nanoprisms possessed higher activity and lower CH_4 selectivity than Co_2C nanospheres.^[17] In addition, the $\text{C}_{5+} + \text{Oxy}$. selectivity increased from 23.9 C% to 68.9 C% as increasing the Mn/Co ratio from 0.33 to 3. The total olefins selectivity and C_{5+} proportion also increased with the increasing of Mn contents (Figure S3), which suggested that Mn promoted the chain growth probability and benefited for the formation of long chain products, especially for high carbon olefins. The CO_2 selectivities for various CoMn catalysts were all above 40 C%, which suggested Co_2C exhibited high WGS

activity and it was suitable for the conversion of syngas derived from coal or biomass with low H_2/CO ratio. Figure 4 showed the change trends of activity and CH_4 selectivity with the proportion of $Co_2C(020)$ facet for various CoMn catalysts. It was clear that lower $Co_2C(020)$ facet proportion would result in lower specific activity and higher CH_4 selectivity. So we can draw conclusion that the Mn content can tune the catalyst activity and CH_4 selectivity via changing the proportion of $Co_2C(020)$ facet of Co_2C nanostructures effectively.

As shown in Table 3 and Figure 5, the O/P ratio in the C_2 - C_4 fraction increased from 1 to 18 as the Mn/Co ratio was raised from 0 to 3, suggesting that the Mn promoter could suppress the second hydrogenation reaction of olefins. The maximum olefins component was C_3 fraction for various CoMn catalysts and C_2 fraction was the lowest as readsorption and second hydrogenation occurred easily for ethylene.

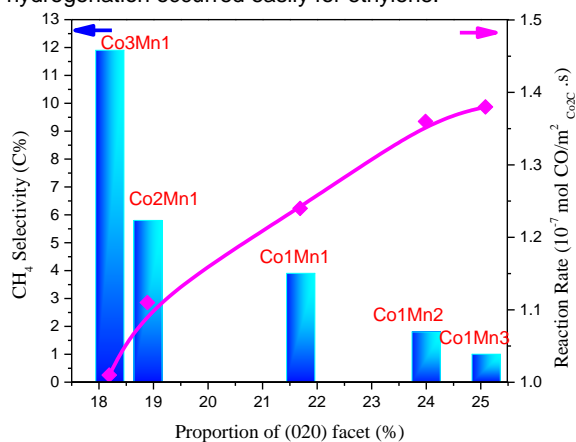


Figure 4. Changes of CH_4 selectivity and reaction rate with proportion of (020) facet for various CoMn catalysts. Reaction conditions: 250 °C, 5 bar, $H_2/CO=0.5$, and WHSV of 2000 $ml \cdot g^{-1} \cdot h^{-1}$.

Figure 6 plotted the hydrocarbon distribution for various CoMn catalysts. For the Co_3O_4 catalyst, the linear fitting of ASF distribution matched well with the conventional ASF distribution trend. As Mn promoter was added into Co-based catalyst, a remarkable deviation from the typical ASF distribution was observed, and the CH_4 value was far below the predicted one. In addition, the degree of deviation from the classical ASF plot increased with increasing of Mn/Co ratio, as the ability for methane formation was greatly suppressed. The hydrocarbon

chain growth factor (α) could be derived from the linear part of the plot and obtained by the component with the carbon number of ≥ 3 , as C_1 and C_2 dropped dramatically from the ideal predicted line. For the Co_3O_4 catalyst, an α value of 0.51 was found and it decreased to 0.33 for Co_3Mn1 . However, the α value increased from 0.33 to 0.46 as Mn/Co ratio improved from 0.33 to 3, which suggested that Mn can enhance the chain growth ability for Co-based FTO reaction.

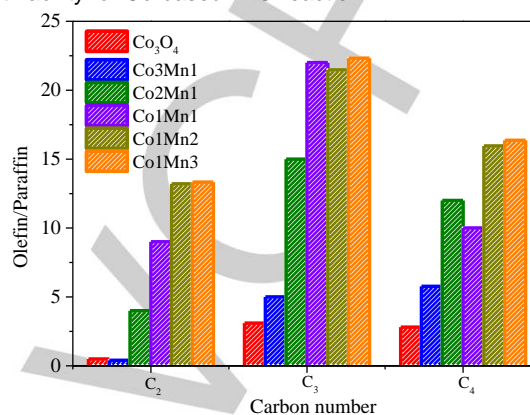


Figure 5. Olefin to paraffin ratio (O/P) within C_2 - C_4 product for various catalysts. Reaction conditions: 250 °C, 5 bar, $H_2/CO=0.5$, and WHSV of 2000 $ml \cdot g^{-1} \cdot h^{-1}$.

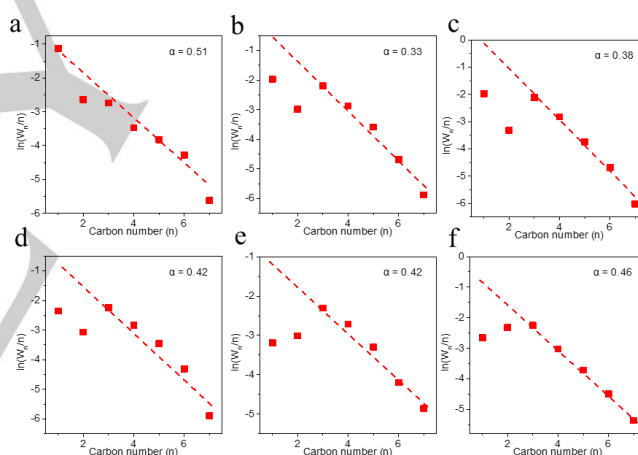


Figure 6. Hydrocarbons plot ($\ln(W_n/n)$ versus n) for various CoMn catalysts with different Mn/Co ratio. a: Co_3O_4 ; b: Co_3Mn1 ; c: Co_2Mn1 ; d: Co_1Mn1 ; e: Co_1Mn2 ; f: Co_1Mn3 . Reaction conditions: 250 °C, 5 bar, $H_2/CO=0.5$, and WHSV of 2000 $ml \cdot g^{-1} \cdot h^{-1}$.

Table 3 Catalytic performance of various CoMn catalysts with different Mn/Co ratio. Co_2C time yield (CTY) represents moles of CO converted to products per gram of Co_2C per second. Reaction rate represents moles of CO converted to products per square meter of Co_2C per second. Reaction conditions: 250 °C, 5bar, $H_2/CO=0.5$, 2000 $ml \cdot g_{cat}^{-1} \cdot h^{-1}$.

Catalyst	CO Conversion (%)	CTY (10^{-6} mol CO/ $g_{Co_2C} \cdot s$)	Reaction rate (10^{-7} mol CO/ $m^2_{Co_2C} \cdot s$)	CO_2 Selectivity (%)	Product selectivity (C%, CO_2 -free)			$C_{2-4}^{\equiv}/C_{2-4}^{\circ}$	
					CH_4	C_{2-4}^{\equiv}	C_{2-4}°	C_{5+} Oxy.	
Co_3O_4	6.1	0.4	0.33	37.6	33.7	33.4	20.4	12.4	1
Co_3Mn1	32.9	7.6	1.01	49.7	11.9	48.0	16.2	23.9	3
Co_2Mn1	28.3	8.2	1.11	46.7	5.8	29.0	2.6	62.4	11
Co_1Mn1	20.4	11.0	1.24	47.9	3.9	28.4	2.0	65.6	14
Co_1Mn2	16.3	12.9	1.36	40.3	1.8	30.6	1.7	66.0	17
Co_1Mn3	9.2	14.2	1.38	45.7	1.0	28.5	1.6	68.9	16

Kinetic study

According to the above results, the catalyst structure and catalytic performance evolved greatly for various catalysts with different Mn content. Thus, it was also necessary to explore the effect of Mn content on kinetic behaviors. As shown in Figure 7, the apparent activation energy (E_a) for CO hydrogenation over the Co_3O_4 catalysts was 224 kJ mol^{-1} , which was obviously higher than other Mn promoted catalysts. Based on the TEM characterization and our previous work, Co_2C nanospheres were obtained for the Co_3O_4 sample, while Co_2C nanoprisms were observed for all of the Mn-promoted catalysts. Co_2C nanoprisms possessed higher activity due to its lower CO dissociation energy barrier.^[17] With increasing Mn/Co ratio from 0.33 to 3, the apparent activation energy for CO hydrogenation decreased gradually from 149 kJ mol^{-1} to 113 kJ mol^{-1} , which suggested that the increase of the proportion of Co_2C (020) facet could decrease the CO dissociation energy barrier.

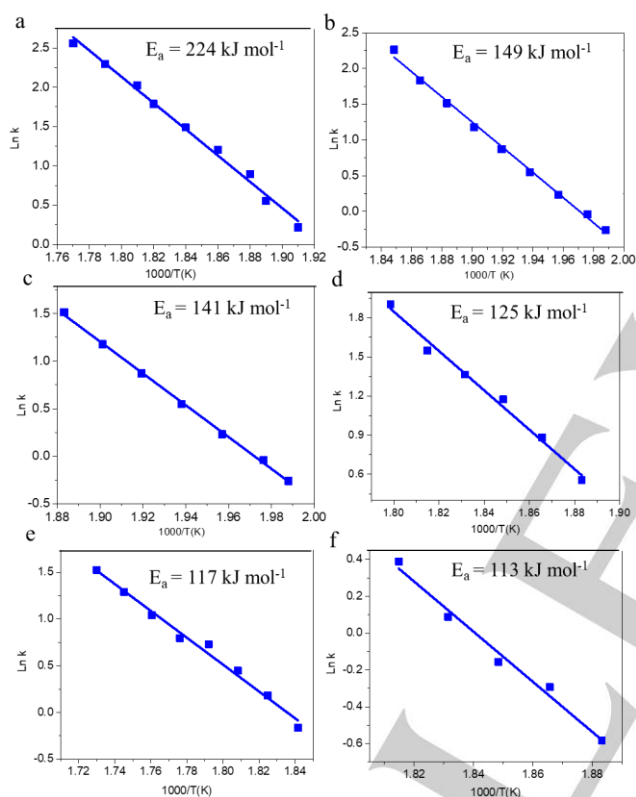


Figure 7. Arrhenius plots for the reaction rate constants (activation energies, E_a) on catalysts with different Mn/Co ratio (a: Co_3O_4 , b: Co_3Mn_1 ; c: Co_2Mn_1 ; d: Co_1Mn_1 ; e: Co_1Mn_2 ; f: Co_1Mn_3).

According to the above study, we found that the addition of Mn could lead to a significant change in catalyst structure and FTO performance. As for pure Co_3O_4 , Co^0 and CoO phases were observed after reduction, while $\text{Co}_x\text{Mn}_{1-x}\text{O}$ could be obtained after introducing Mn into Co-based catalysts. Our previous work has already demonstrated that the $\text{Co}_x\text{Mn}_{1-x}\text{O}$ spinel phase played a vital role for the formation of Co_2C nanoprisms with exposed (101) and (020) facet. The absence of Mn promoter for Co_3O_4 caused the formation of Co_2C nanospheres with (111) as dominant facet via carburization of Co^0 and CoO route, which restrained the CO dissociation and favored the production of methane. In addition, the intrinsic activity was the lowest when Co_2C nanospheres with (111) facet were formed. The H_2 -TPR

results showed that the Mn promoter would hinder the reducibility of Co species because of the formation of a stable Co-Mn spinel,^[19] and the XRD results also indicated that only $\text{Co}_x\text{Mn}_{1-x}\text{O}$ was obtained at the selected reduction temperature. In addition, the crystallite size of Co_2C nanoprisms decreased with increasing Mn/Co ratio due to the confinement effect of Mn. The as-obtained results illustrated that the specific surface area proportion of (020) facet in the total exposed facets increased rapidly, and it could be fine-tuned by controlling the Mn content. Based on DFT calculation results, direct ($\text{CO} \rightarrow \text{C} + \text{O}$) CO dissociation was easier occurred on Co_2C . For the flat- and stepped- $\text{Co}_2\text{C}(020)$ surfaces, the calculated CO direct dissociation barriers were 1.76 and 1.34 eV,^[17] respectively. In addition, the values were 2.16 and 2.18 eV for the flat- and stepped- $\text{Co}_2\text{C}(101)$, and 2.18 and 2.16 eV for the flat- and stepped- $\text{Co}_2\text{C}(111)$ surfaces^[20]. It was suggested that CO was much easier dissociated directly on $\text{Co}_2\text{C}(020)$. Besides, for the CH_4 formation, the values of $E_{\text{eff,CH}_4}$ were 2.88, 3.44 eV on the flat- and stepped- $\text{Co}_2\text{C}(020)$, which was higher than that on the $\text{Co}_2\text{C}(101)$ and $\text{Co}_2\text{C}(111)$ surfaces (1.06 and 2.11 eV for the flat- and stepped- $\text{Co}_2\text{C}(101)$, 2.13 and 0.62 eV for the flat- and stepped- $\text{Co}_2\text{C}(111)$). Obviously, CH_4 was more difficult to be formed on the $\text{Co}_2\text{C}(020)$ facet than $\text{Co}_2\text{C}(101)$ and $\text{Co}_2\text{C}(111)$ facet.^[17] Therefore, the CoMn catalyst with a larger surface area proportion of (020) facet exhibited higher intrinsic activity for CO conversion and lower methane selectivity, as illustrated in Figure 4. The kinetic experiment further elucidates the underlying reason for the changes in intrinsic activity. It was found that the apparent activation energy of CO hydrogenation continuously decreased from 149 kJ mol^{-1} to 113 kJ mol^{-1} as Mn/Co ratio increased from 0.33 to 3. The variation of apparent activation energy reflected the CO activation ability of Co_2C , and it can be further ascribed to the difference in the surface area proportion of (020) facet.

Conclusion

The influence of Mn promoter on tuning the exposed facet proportion of Co_2C as well as the corresponding FTO performance were investigated in detail. Co_2C nanospheres with (111) as dominant facet were found for the Co_3O_4 sample. The addition of Mn into the Co-based catalysts caused a significant change in catalyst structure and catalytic performance. $\text{Co}_x\text{Mn}_{1-x}\text{O}$ spinel phase instead of MnO and Co^0 was observed for CoMn samples after reduction, and Co_2C nanoprisms with (020) and (101) exposed facets gradually evolved under FTO reaction conditions. Besides, the specific surface area proportion of $\text{Co}_2\text{C}(020)$ facet in the total exposed facet as well as the relative intensity ratio of (020)/(101) increased with increasing of Mn/Co ratio. With the increase of specific surface area proportion of $\text{Co}_2\text{C}(020)$ in nanoprisms, the intrinsic activity for CO conversion also increased and the methane formation was greatly suppressed. Kinetic experiments further verified that the apparent activation energy (E_a) for CO conversion decreased from 149 kJ mol^{-1} to 113 kJ mol^{-1} with increasing surface area proportion of $\text{Co}_2\text{C}(020)$ facet. Above all, this work demonstrated that the Co_2C morphology and the preferential exposed (020) facet proportion can be effectively tuned by adjusting the Mn/Co ratio, and it may provide a feasible way for the rational design of Co_2C nanocatalysts for FTO reaction.

Experimental Section

Catalyst preparation

CoMn catalysts with different molar Co/Mn ratio (Co_xMn_y , x/y denoted the molar of Co/Mn ratio and it was controlled with 0, 0.33, 0.5, 1, 2 and 3, respectively) were synthesized via co-precipitation method using aqueous solutions of cobalt nitrate ($(\text{Co}(\text{NO}_3)_2 \cdot 6\text{H}_2\text{O})$), manganese nitrate (50 wt % $\text{Mn}(\text{NO}_3)_2$) as the precursor salts, and sodium carbonate (Na_2CO_3) as the precipitate, and they were all purchased from Sinopharm Chemical Reagent Co, Ltd. The solution containing 2 M total metal ions (Co^{2+} and Mn^{2+}), and 2 M Na_2CO_3 were added simultaneously into the mother solution (100 ml deionized water) under strong stirring with rotational speed 260 rpm. The pH of the solution was fixed at about 8, and the temperature of the water bath was kept at about 30 °C. After co-precipitation, the as-prepared mixture was aged at 30 °C for 2 h under continuous stirring, then washed for several times until the pH value reached ca. 7.0. The as-obtained samples were dried at 120 °C for 10 h and then calcined at 330 °C for 3 h at atmospheric pressure. The calcined catalysts were reduced under flowing atmosphere with 10 vol % CO/N_2 (200 ml/min) at 300 °C for 5 h. The reduced samples were passivated with 1 vol % O_2/Ar for 70 minutes at room temperature for structure characterization. The spent samples were removed from the reactor after similar passivation process for structure characterization

Catalyst characterization

The actual compositions of the catalysts were determined with a Varian 710-ES Inductively Coupled Plasma Atomic Emission Spectrometer (ICP-OES, Optima 8000, PerkinElmer).

Nitrogen adsorption measurements were performed on a Micromeritics TriStar 3020 instrument at -196 °C. 50 mg sample was prepared to load in a tube and then degassed at 200 °C in vacuum for 6 h. Brunauer-Emmett-Teller (BET) method was used to calculate the specific area. The total pore volume and the average pore size were determined using Barrett-Joyner-Halenda (BJH) method.

H_2 -temperature programmed reduction (TPR) profiles were collected on a tp-5080 equipment with 30 mg sample loaded in a U-tube. During the TPR process, 5 vol % H_2/Ar with flow of 30 mL/min was introduced at the temperature ranged from 50–800 °C with a ramping of 10 °C/min.

X-ray diffraction (XRD) patterns were recorded on a Rigaku Ultima IV X-ray powder diffractometer using Cu K α radiation that the wavelength (λ) was 1.54056 Å, operated at 40 kV and 40 mA. The scanning angle (2θ) was ranging from 30 - 80°. The average crystallite size was estimated using the Scherrer equation with the strongest diffraction peaks. The phases were identified by comparing the observed patterns with JCPDS standard files.

The content of different phases was calculated by means of Rietveld refinement using the GSAS-II program [21]. Structural data for the Co_2C , MnO , MnCO_3 and $\text{Co}_x\text{Mn}_{1-x}\text{O}$ phases were taken from the Inorganic Crystal Structure Database (ICSD, accession numbers 16895, 643195, 28556 and 9865, respectively). Lattice parameters for Co_2C and MnO were predetermined in a separate refinement and kept fixed during the refinements. For all specimens, the scale factors, profile shape and broadening parameters, asymmetry and corrections for the preferred orientation were refined during the quantitative analysis. Besides, the parameters of Co_2C were calculated by the MDI Jade 6 software. According to half-width of the diffraction peak in the XRD, similarly to the crystallite sizes, the edge length of the Co_2C nanoprism particles were deduced from the Scherrer equation. The strongest diffraction peak at $2\theta = 42.57^\circ$ was used to calculate the crystal size based on the Scherrer equation. Edge length in the model as showed in Figure S2 was calculated by peaks at $2\theta = 41.28^\circ$ and 37.01° . The relative (I/I_p) was

used to estimate the relative numbers of exposed facets, where I is the diffraction intensity and L_p is the diffraction angle factor, which are described as following [18]:

$$L_p = (1 + \cos^2 2\theta) / \sin 2\theta \cos \theta$$

Transmission electron microscopy (TEM) characterization was carried out on a JEOL JEM 2011 electron microscope, equipped with 200 kV accelerating voltage. Samples for TEM test were prepared by dispersing the powder in ethanol followed by ultrasonication. One droplet of the suspension was dripped onto carbon-coated copper grids for measurement. Spatial drift was corrected with a simultaneous image collector.

Catalytic evaluation

Syngas conversion was carried out on a continuous flow fixed bed reactor. Generally, 1.5 g catalyst of 40-60 mesh mixed physically with 3 g silica sand with the same size were all loaded into a stainless steel reactor with inner diameter of 9 mm. Prior to the reaction, the catalyst was reduced in situ 10 vol % CO/N_2 at 300 °C for 5 h under atmosphere pressure. After reduction, the temperature then dropped to 250 °C in He (99.999 vol %) flow to purge the residual reduction gas. Subsequently, the He was switched to a mixture of 97 vol % syngas ($\text{H}_2/\text{CO}=0.5$, v/v) and 3 vol % N_2 as internal standard in the reactor as feed gas. A system pressure of 5 bar and a WHSV of 2000 ml/h- g_{cat} were adopted for catalytic reaction. The outlet gas, after passing through the hot trap (120 °C) and cold trap (0 °C), was immediately analyzed online by gas chromatograph (GC, Agilent 7890B). H_2 , N_2 , CO , CH_4 , and CO_2 were analyzed through a carbon molecular sieves column (TDX-1) with a thermal conductivity detector (TCD), and the He was used as the carrier gas. C_1 to C_{10} hydrocarbons were analyzed through a KCl modified alumina capillary column (19095P-K25) with Ar carrier and hydrogen flame ionization detector (FID). The CO conversion was calculated according to the internal standard method, assuming that the N_2 amount remained constant after reaction. The aqueous products, oil products and wax products, collected from cold trap and hot trap, were analyzed off-line by Shimadzu GC. The activation energy was measured via changing the reaction temperature at atmosphere pressure. In the process of studying activation energy (E_a), we chose the suitable velocity to adjust the catalyst activity and avoided the diffuse effects.

The catalytic activity and products selectivity were calculated according to the following formula:

CO conversion was calculated according to eq 1:

$$\text{CO Conversion} = \frac{\text{CO}_{\text{inlet}} - \text{CO}_{\text{outlet}}}{\text{CO}_{\text{inlet}}} \times 100\% \quad (1)$$

CO_2 selectivity was calculated according to eq 2:

$$\text{CO}_2 \text{ Selectivity} = \frac{\text{CO}_2 \text{ outlet}}{\text{CO}_{\text{inlet}} - \text{CO}_{\text{outlet}}} \times 100\% \quad (2)$$

CTY (Co_2C time yield) calculation was based on mass of the active sites according to eq 3:

$$\text{CTY} = \frac{n_{\text{CO Conversion}}}{m_{\text{active sites}}} \times 100\% \quad (3)$$

Reaction rates were normalized by surface area of the active phase according to eq 4:

$$\text{Reaction rate} = \frac{\text{CTY}}{S_{\text{active sites}}} \times 100\% \quad (4)$$

The selectivity of the individual product (hydrocarbon or oxygenate) C_nH_m (CO_2 -free) was obtained according to eq 5:

$$C_nH_m \text{ Selectivity} = \frac{nC_nH_m \text{ outlet}}{CO_{inlet} - CO_{outlet} - CO_2 \text{ outlet}} \times 100\% \quad (5)$$

The C_{5+} represents hydrocarbons with 5 or more carbons and Oxy. denotes oxygenates and it was obtained according to eq 6:

$$(C_{5+} + \text{Oxy.}) \text{ Selectivity} = 100\% - CO_2 \text{ Selectivity} - C_{1-4} \text{ Selectivity} \quad (6)$$

Where CO_{inlet} and CO_{outlet} represented moles of CO at the inlet and outlet, $CO_2 \text{ outlet}$ and $C_nH_m \text{ outlet}$ represented moles C of CO_2 and hydrocarbons at the outlet, and Oxy. refers to oxygenate products (mainly aldehydes and alcohols). $m \text{ active sites}$ was calculated based on the quantitative Rietveld refinement of XRD. $S \text{ active sites}$ was calculated based on the Scherrer equation and nanostructure of active phase. The detailed analysis procedure could be found in our previous literatures.^[13]

Acknowledgements

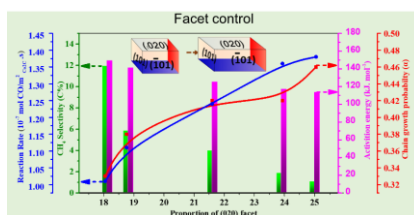
This work was supported by the Ministry of Science and Technology of China (2016YFA0202802), Natural Science Foundation of China (21573271, 91545112, 21703278, and 21776296), Key Research Program of Frontier Sciences, CAS (Grant No. QYZDB-SSW-SLH035), the "Transformational Technologies for Clean Energy and Demonstration", Strategic Priority Research Program of the Chinese Academy of Sciences (Grant No. XDA21020600) and the Youth Innovation Promotion Association of CAS.

Keywords: Syngas conversion 1, Fischer-Tropsch synthesis 2, Fischer-Tropsch to olefins 3, Facet effect 4, CO_2 C 5

- [1] a) D. I. Foustoukos, W. E. Seyfried, *Science* **2004**, *304*, 1002-1005; b) J. Horita, M. E. Berndt, *Science* **1999**, *285*, 1055-1057; c) Y. Pei, Y. Ding, H. Zhu, D. Hong, *Chinese J. Catal.* **2015**, *36*, 355-361.
- [2] a) S. Abelló, D. Montané, *Chemsuschem* **2011**, *4*, 1538-1556; b) X. P. Fu, Q. K. Shen, D. Shi, K. Wu, Z. Jin, X. Wang, R. Si, Q. S. Song, C. J. Jia, C. H. Yan, *Appl. Catal. B Environ.* **2017**, *211*, 176-187; c) S. Zarubova, S. Rane, J. Yang, Y. Yu, Y. Zhu, D. Chen, A. Holmen, *Chemsuschem* **2011**, *4*, 935-942; d) W. Niemantsverdriet, A. M. V. D. Kraan, *J. Catal.* **1981**, *72*, 385-388.
- [3] W. Chen, T. Lin, Y. Dai, Y. An, F. Yu, L. Zhong, S. Li, Y. Sun, *Catal. Today* **2018**, *311*, 8-22.
- [4] T. Herranz, S. Rojas, F. J. Pérez-Alonso, M. Ojeda, P. Terreros, J. L. G. Fierro, *J. Catal.* **2006**, *243*, 199-211.
- [5] J. X. Liu, H. Y. Su, D. P. Sun, B. Y. Zhang, W. X. Li, *J. Am. Chem. Soc.* **2013**, *135*, 16284-16287.
- [6] a) F. Jiao, J. Li, X. Pan, J. Xiao, H. Li, H. Ma, M. Wei, Y. Pan, Z. Zhou, M. Li, S. Miao, J. Li, Y. Zhu, D. Xiao, T. He, J. Yang, F. Qi, Q. Fu, X. Bao, *Science* **2016**, *351*, 1065-1068; b) K. Cheng, B. Gu, X. Liu, J. Kang, Q. Zhang, Y. Wang, *Angew. Chem., Int. Ed.* **2016**, *55*, 1-5.
- [7] a) Y. Cheng, J. Lin, K. Xu, H. Wang, X. Yao, Y. Pei, S. Yan, M. Qiao, B. Zong, *Acs Catalysis* **2016**, *6*; b) B. Gu, A. Y. Khodakov, V. V. Ordonsky, *Chem. Commun.* **2018**, *54*, 2345; c) E. Ø. Pedersen, I. H. Svernum, E. A. Blekkan, *J. Catal.* **2018**, *361*, 23-32.
- [8] H. M. Torres Galvis, J. H. Bitter, C. B. Khare, M. Ruitenbeek, A. I. Dugulan, K. P. de Jong, *Science* **2012**, *335*, 835-838.
- [9] H. M. Torres Galvis, A. C. J. Koeken, J. H. Bitter, T. Davidian, M. Ruitenbeek, A. I. Dugulan, K. P. de Jong, *J. Catal.* **2013**, *303*, 22-30.
- [10] P. Zhai, C. Xu, R. Gao, X. Liu, M. Li, W. Li, X. Fu, C. Jia, J. Xie, M. Zhao, *Angew. Chem., Int. Ed.* **2016**, *55*, 9902.

- [11] Y. Liu, J. F. Chen, J. Bao, Y. Zhang, *ACS Catal.* **2015**, *5*, 3905-3909.
- [12] a) G. L. Bezemer, P. B. Radstake, U. Falke, H. Oosterbeek, H. P. C. E. Kuipers, A. J. V. Dillen, K. P. de Jong, *J. Catal.* **2006**, *237*, 152-161; b) J. H. D. Otter, K. P. de Jong, *Top. Catal.* **2014**, *57*, 445-450; c) G. J. Hutchings, R. G. Copperthwaite, M. V. D. Riet, *Top. Catal.* **1995**, *2*, 163-172; d) R. G. Copperthwaite, G. J. Hutchings, M. V. D. Riet, J. Woodhouse, *Ind. Eng. Chem. Res.* **1987**, *26*, 18-19; e) T. E. Feltes, Y. Zhao, R. F. Klie, R. J. Meyer, J. R. Regalbuto, *Chemcatchem* **2010**, *2*, 1065-1068; f) M. Mansouri, H. Atashi, F. F. Tabrizi, A. A. Mirzaei, G. Mansouri, *Ind. Eng. Chem.* **2013**, *19*, 1177-1183; g) F. Morales, E. D. Smit, F. M. F. D. Groot, T. Visser, B. M. Weckhuysen, *J. Catal.* **2007**, *246*, 91-99; h) J. Ming, N. Koizumi, T. Ozaki, M. Yamada, *Appl. Catal. A Gen.* **2001**, *209*, 59-70; i) E. Iglesia, *Appl. Catal. A Gen.* **1997**, *161*, 59-78.
- [13] L. Zhong, F. Yu, Y. An, Y. Zhao, Y. Sun, Z. Li, T. Lin, Y. Lin, X. Qi, Y. Dai, L. Gu, J. Hu, S. Jin, Q. Shen, H. Wang, *Nature* **2016**, *538*, 84-87.
- [14] a) J. C. Mohandas, M. K. Gnanamani, G. Jacobs, W. Ma, Y. Ji, S. Khalid, B. H. Davis, *ACS Catal.* **2011**, *1*, 1581-1588; b) Cheng, P. Hu, *J. Phys. Chem. C* **2010**, *114*, 1085-1093; c) H. Karaca, O. V. Safonova, S. Chambrey, P. Fongarland, P. Roussel, A. Griboval-Constant, M. Lacroix, A. Y. Khodakov, *J. Catal.* **2011**, *277*, 14-26; d) M. Claeys, M. E. Dry, E. V. Steen, E. D. Plessis, P. J. V. Berge, A. M. Saib, D. J. Moodley, *J. Catal.* **2014**, *318*, 193-202; e) G. Kwak, H. W. Min, S. C. Kang, H. G. Park, Y. J. Lee, K. W. Jun, K. S. Ha, *J. Catal.* **2013**, *307*, 27-36.
- [15] Z. Li, L. Zhong, F. Yu, Y. An, Y. Dai, Y. Yang, T. J. Lin, S. Li, H. Wang, P. Gao, *ACS Catal.* **2017**, *7*, 3622-3631
- [16] Z. Li, T. Lin, F. Yu, Y. An, Y. Dai, S. Li, L. Zhong, H. Wang, P. Gao, Y. Sun, *Acs Catalysis* **2017**, *7*, 8023-8032.
- [17] Y. An, F. Yu, T. Lin, Y. Lu, S. Li, Z. Li, Y. Dai, X. Wang, H. Wang, L. Zhong, Y. Sun, *J. Catal.* **2018**, *366*, 289-299.
- [18] B. H. Toby, R. B. V. Dreele, *J. Appl. Crystal.* **2013**, *46*, 544-549.
- [19] C. Huo, B. Wu, P. Gao, Y. Yang, Y. Li, H. Jiao, *Angew. Chem., Int. Ed.* **2011**, *50*, 7403-7406.
- [20] a) K. Guse, H. Papp, *Fresenius J. Anal. Chem.* **1993**, *346*, 84-91; b) H. G. Salazar-Contreras, A. Martínez-Hernández, A. A. Boix, G. A. Fuentes, E. Torres-García, *Appl. Catal. B Environ.* **2019**, *244*, 414-426.
- [21] Y. Pei, J. Liu, Y. Zhao, Y. Ding, T. Liu, W. Dong, H. Zhu, H. Su, L. Yan, J. Li, W. Li, *ACS Catal.* **2015**, *5*, 3620-3624.

Entry for the Table of Contents



The facet proportion of Co₂C nanoprism was tuned effectively for direct production of lower olefins from syngas.